References

1 Amarenco P, Cohen A, Tzourio C, Bertrand B, Hommel M, Besson G, Chauvel C, Touboul PJ, Bousser MG: Atherosclerotic disease of the aortic arch and the risk of ischemic stroke. N Engl J Med 1994;331:1474–1479.

2 The French Study of Aortic Plaques in Stroke Group: Atherosclerotic disease of the aortic arch as a risk factor for recurrent ischemic stroke. The French Study of Aortic Plaques in Stroke Group. N Engl J Med 1996;334:1216–1221.

3 Mitusch R, Doherty C, Wucherpfennig H, Memmesheimer C, Tepe C, Stierle U, Kessler C, Sheikhzadeh A: Vascular events during follow-up in patients with aortic arch atherosclerosis. Stroke 1997;28:36–39.

4 Tunick PA, Nayar AC, Goodkin GM, Mirchandani S, Francescone S, Rosenzweig BP, Freedberg RS, Katz ES, Applebaum RM, Kronzon I: Effect of treatment on the incidence of stroke and other emboli in 519 patients with severe thoracic aortic plaque. Am J Cardiol 2002;90:1320–1325.

5 Amarenco P, Duyckaerts C, Tzourio C, Henin D, Bousser MG, Hauw JJ: The prevalence of ulcerated plaques in the aortic arch in patients with stroke. N Engl J Med 1992;326:221–225.

6 Fujimoto S, Yasaka M, Otsubo R, Oe H, Nagatsuka K, Minematsu K: Aortic arch atherosclerotic lesions and the recurrence of ischemic stroke. Stroke 2004;35:1426–1429.

7 Jones EF, Kalman JM, Calafiore P, Tonkin AM, Donnan GA: Proximal aortic atheroma. An independent risk factor for cerebral ischemia. Stroke 1995;26:218–224.

8 Toyoda K, Yasaka M, Nagata S, Yamaguchi T: Aortogenic embolic stroke: A transesophageal echocardiographic approach. Stroke 1992;23:1056–1061.

9 Kazui S, Levi CR, Jones EF, Quang L, Calafiore P, Donnan GA: Lacunar stroke: transoesophageal echocardiographic factors influencing long-term prognosis. Cerebrovasc Dis 2001;12:325–330.

10 Yamaguchi T, Minematsu K, Choki J, Ikeda M: Clinical and neuroradiological analysis of thrombotic and embolic cerebral infarction. Jpn Circ J 1984;48:50–58.

11 Special report from the National Institute of Neurological Disorders and Stroke. Classification of cerebrovascular diseases III. Stroke 1990;21:637–676.

12 Gupta V, Nanda NC, Yesilbursa D, Huang WY, Li Q, Gomez CR: Racial differences in thoracic aorta atherosclerosis among ischemic stroke patients. Stroke 2003;34:408–412.

13 Di Tullio MR, Sacco RL, Savoia MT, Sciacca RR, Homma S: Aortic atheroma morphology and the risk of ischemic stroke in a multiethnic population. Am Heart J 2000;139:329–336.

14 Kieffer SA, Takeya Y, Resch JA, Amplatz K: Racial differences in cerebrovascular disease: angiographic evaluation of Japanese and American populations. Am J Roentgenol Radium Ther Nucl Med 1967;101:94–99.

15 Leung SY, Ng TH, Yuen ST, Lauder IJ, Ho FC: Pattern of cerebral atherosclerosis in Hong Kong Chinese: severity in intracranial and extracranial vessels. Stroke 1993;24:779–786.

16 Liu HM, Tu YK, Yip PK, Su CT: Evaluation of intracranial and extracranial carotid stenoocclusive diseases in Taiwan Chinese patients with MR angiography: preliminary experience. Stroke 1996;27:650–653.

17 Suh DC, Lee SH, Kim KR, Park ST, Lim SM, Kim SJ, Choi CG, Lee HK: Pattern of atherosclerotic carotid stenosis in Korean patients with stroke: different involvement of intracranial versus extracranial vessels. AJNR 2003;24:239–244.

18 Wong KS, Huang YN, Gao S, Lam WW, Chan YL, Kay R: Intracranial stenosis in Chinese patients with acute stroke. Neurology 1998;50:812–813.

19 Rundek T, Di Tullio MR, Sciacca RR, Titova IV, Mohr JP, Homma S, Sacco RL: Association between large aortic arch atheromas and high-intensity transient signals in elderly stroke patients. Stroke 1999;30:2683–2686.

20 Castellanos M, Serena J, Segura T, Perez-Ayuso MJ, Silva Y, Davalos A: Atherosclerotic aortic arch plaques in cryptogenic stroke: a microembolic signal monitoring study. Eur Neurol 2001;45:145–150.

21 Viguier A, Pavy le Traon A, Massabuau P, Valton L, Larrue V: Asymptomatic cerebral embolic signals in patients with acute cerebral ischaemia and severe aortic arch atherosclerosis. J Neurol 2001;248:768–771.

22 Cohen A, Tzourio C, Bertrand B, Chauvel C, Bousser MG, Amarenco P: Aortic plaque morphology and vascular events: a follow-up study in patients with ischemic stroke. FAPS Investigators. French Study of Aortic Plaques in Stroke. Circulation 1997;96:3838–3841.

Annals of Nuclear Medicine Vol. 20, No. 3, 245–251, 2006

System design and development of a pinhole SPECT system for quantitative functional imaging of small animals

Toshiyuki AOI,*,** Tsutomu ZENIYA,* Hiroshi WATABE,* Hossain M. DELOAR,* Tetsuya MATSUDA** and Hidehiro IIDA*

*Department of Investigative Radiology, National Cardiovascular Center Research Institute
**Department of System Science, Graduate School of Informatics, Kyoto University

Recently, small animal imaging by pinhole SPECT has been widely investigated by several researchers. We developed a pinhole SPECT system specially designed for small animal imaging. The system consists of a rotation unit for a small animal and a SPECT camera attached with a pinhole collimator. In order to acquire complete data of the projections, the system has two orbits with angles of 90° and 45° with respect to the object. In this system, the position of the SPECT camera is kept fixed, and the animal is rotated in order to avoid misalignment of the center of rotation (COR). We implemented a three dimensional OSEM algorithm for the reconstruction of data acquired by the system from both the orbitals. A point source experiment revealed no significant COR misalignment using the proposed system. Experiments with a line phantom clearly indicated that our system succeeded in minimizing the misalignment of the COR. We performed a study with a rat and ^{99m}Tc-HMDP, an agent for bone scan, and demonstrated a dramatic improvement in the spatial resolution and uniformity achieved by our system in comparison with the conventional Feldkamp algorithm with one set of orbital data.

Key words: pinhole SPECT, complete data acquisition, small animal imaging

INTRODUCTION

IN VIVO IMAGING of physiological functions (e.g., the tissue blood flow and receptor binding potentials) in small laboratory animals facilitates the objective assessment of pharmaceutical development and regenerative therapy in pre-clinical trials. Micro positron emission tomography (PET) has been extensively emphasized for achieving high spatial resolution in the imaging of small animals, which approaches 1.0 mm.[1–3] An alternative methodology for small animal imaging is micro single photon emission computed tomography (micro SPECT) in which a camera is fitted with a pinhole collimator.[4–8] Pinhole SPECT has low sensitivity as compared with small animal PET; however, depending on the size of the pinhole, the spatial resolution achieved by pinhole SPECT can exceed that of PET. Unlike PET systems, the pinhole SPECT system does not require a cyclotron for producing radiopharmaceuticals, and it has an excellent cost/performance ratio. Moreover, the half life of radiopharmaceuticals used for pinhole SPECT is relatively longer than that used for PET, which is beneficial in investigating slow pharmacokinetics.

In addition to the lower sensitivity of pinhole SPECT, the existence of image distortion in the axial direction and non-uniform spatial resolution in the reconstructed image for the pinhole SPECT are also areas of concern. One explanation for this non-uniformity is due to incompleteness of data and use of Feldkamp filtered backprojection (FBP) algorithm as an approximate 3D FBP.[9] This non-unifomity can be suppressed by applying statistical reconstruction algorithms such as maximum likelihood expectation maximization (MLEM)[10,11] or ordered subsets expectation maximization (OSEM),[12] but in the periphering of FOV, the

Received June 30, 2005, revision accepted December 13, 2005.

For reprint contact: Toshiyuki Aoi, R.T., Department of Investigative Radiology, National Cardiovascular Center Research Institute, 5-7-1 Fujishiro-dai, Suita, Osaka 565-8565, JAPAN.
E-mail: toshiaoi@ri.ncvc.go.jp

image is blurred.[5,13] This non-uniformity of the image resolution often hampers further quantitative analysis. Tuy showed that in order to obtain a strict three-dimensional (3D) tomogram in cone-beam CT, the following geometric condition should be fulfilled: "all the planes that cross an object cross the axis of the X-ray source."[14,15] Tuy's condition can be adapted to pinhole SPECT. The conventional pinhole SPECT with one circular orbit does not fulfill this condition. Kudo and Saito suggested examples of orbits that can satisfy Tuy's condition: use of two circular orbits, a spiral orbit, or a single circular orbit in conjunction with a straight line.[16-18] By satisfying Tuy's condition, Zeniya et al. demonstrated an improvement in the uniformity of the spatial resolution of pinhole SPECT by using two circular orbits with angles of 90° and 45° with respect to the object.[19] However, they did not present details of a system configuration including hardware and software. In this paper, we focused on the detailed descriptions of system (hardware as well as software) which is able to properly acquire data from two circular orbits.

MATERIALS AND METHODS

System configuration

The misalignment of the center of rotation (COR) could be more critical for data acquisition with two orbits as compared with a single orbital system. Therefore, in the proposed system, the detector and collimator were fixed, and the small animal was rotated. The outline of the system and the data flowchart are shown in Figure 1. This system consists of a rotation unit (RU), rotation unit control board (RU controller), pinhole collimator, and SPECT camera.

Rotation unit (RU)

A small animal was rotated on the RU (Fig. 2), which consisted of a base-board and a rotating stage. The rotating stage was driven by a stepping motor (SGSP-120YAW-θz, Sigma Company, Tokyo, Japan) with a COR accuracy of 20 μm. As shown in Figure 2, the small animal can be fixed in the direction of either 90° or 45°. The axes of the two directions intersect each other, and the distances between the intersection point and each base are equal ($T1 = T2$). In order to perform data acquisition with two circular orbits, the intersection point must coincide with the COR of the pinhole detector, i.e., the line perpendicular to the detector center should cross the intersection point, as shown in Figure 2. An adjustment implement (Fig. 3) was utilized to achieve this. The implement was designed to position a radioactive point source at the COR. Then, the COR was adjusted by acquiring data with the point source for various angle directions.

The rat holder was prepared such that the femoral parts and tail of the rat would lie out of the holder (Fig. 4). It was fabricated from 0.5 mm-thick vinyl chloride.

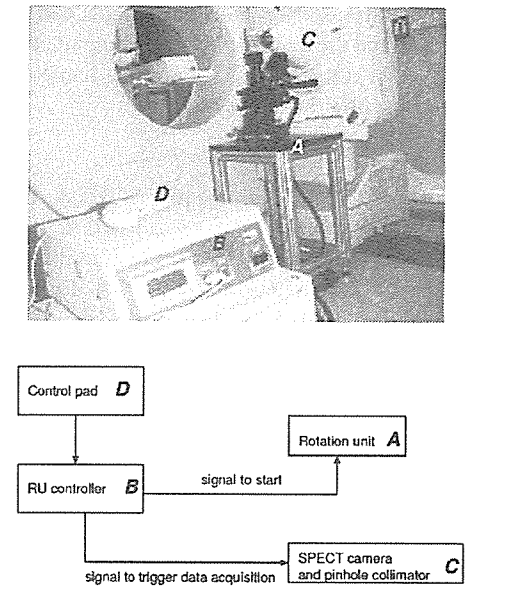

Fig. 1 *Upper:* Overview of the proposed pinhole SPECT system for small animals. *Lower:* Schematic diagram of the system. (A) rotation unit (RU), (B) RU controller, (C) SPECT camera and pinhole collimator, and (D) control pad.

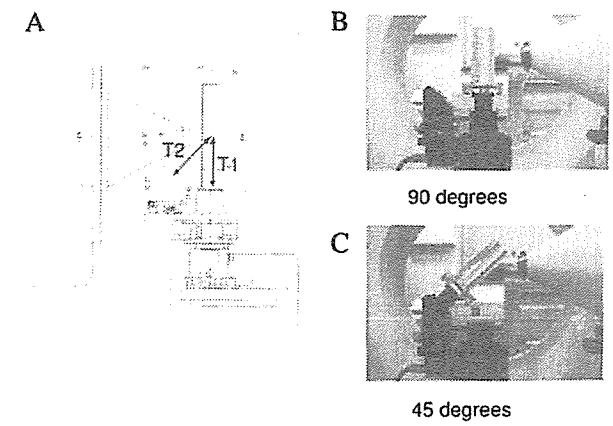

Fig. 2 Cross section of the rotation unit (A) and schematic views of the 90° orbit (B) and 45° orbit (C).

RU controller

In order to control the RU, a general-purpose controller (Mark202, Sigma Company, Tokyo, Japan) was employed. The RU controller could control the starting point of the stepping motor, rotation direction, step angle, and speed of rotation using a control pad. The minimum amount of movements per pulse was 0.01° and the maximum speed of movement was 100°/s.

Pinhole collimator

The pinhole collimator (NDCL709A, Toshiba, Tokyo, Japan) used had a tungsten knife-edge head, which was replaceable. The available hole sizes were 0.25 mm, 0.5

mm, 1 mm, 2 mm, and 4.8 mm. The pinhole had an open angle of 60°, and the distance between the pinhole center and the detector surface was 251 mm. The diameter of the bottom of the collimator was 288 mm.

SPECT camera

A clinically used SPECT camera (GCA-7100A, Toshiba, Tokyo, Japan) with one detector was used. As shown in Figure 1, the camera stayed in one position during data acquisition. The acquired projection data had a matrix of size 128 × 128, and the pixel size 4.3 × 4.3 mm^2.

In order to enable data acquisition with the proposed system, the software installed in GCA-7100A was modified to receive a signal from the RU controller. A signal was sent to the RU to begin rotation with a particular stepping angle. After that rotation, a trigger signal was sent to GCA-7100A to acquire the projection data (See Fig. 1). The above process was repeated until the RU completed 360° rotation.

Image reconstruction

We developed a 3D OSEM algorithm for reconstructing the projection data-set acquired with two different circular orbits.[19] Figure 5 describes the coordinates for the 3D reconstruction with the proposed pinhole SPECT system based on two circular orbits, which are defined as (x, y, z), (x', y', z'), and (x'', y'', z''). The radioactivity concentration of the object is expressed within a fixed (x, y, z) system as $f(x, y, z)$. The second coordinate system (x', y', z') represents the tilt of the (x, y, z) system about the y axis with an oblique angle of ϕ. The third coordinate system (x'', y'', z'') is a rotational coordinate system where (x', y', z') rotates around the z axis with an angle θ. The tilt of (x, y, z) by the angle ϕ produces the following transformations:

$$\begin{pmatrix} x' \\ y' \\ z' \end{pmatrix} = R_1 \begin{pmatrix} x \\ y \\ z \end{pmatrix}, R_1 = \begin{pmatrix} \cos\phi & 0 & \sin\phi \\ 0 & 1 & 0 \\ -\sin\phi & 0 & \cos\phi \end{pmatrix} \quad (1)$$

Similar to Eq. (1), which represents the transformation between the (x, y, z) and (x', y', z') coordinates, the following equation expresses that between the (x, y, z) and (x'', y'', z'') coordinates:

$$\begin{pmatrix} x'' \\ y'' \\ z'' \end{pmatrix} = R_2 \begin{pmatrix} x' \\ y' \\ y' \end{pmatrix} = R_2 R_1 \begin{pmatrix} x \\ y \\ z \end{pmatrix}, R_2 = \begin{pmatrix} \cos\theta & -\sin\theta & 0 \\ \sin\theta & \cos\theta & 0 \\ 0 & 0 & 1 \end{pmatrix} \quad (2)$$

In case of $\phi = 0$, the geometry of the system equals that of conventional pinhole SPECT with one circular orbit.[20,21] Therefore, for reconstruction with an oblique orbit, a procedure similar to conventional pinhole SPECT can be applied using Eq. 2. The source voxel (x_1'', y_1'', z_1'') is projected toward the detector thorough the pinhole collimation of the oblique circular orbit, as shown in Figure 6. We denote the detector plane and a plane parallel to it that includes the source voxel as Plane 1 and Plane 2, respectively. The source point $(t_x, t_z) = (x_1'', z_1'')$ on Plane 2 is the projected point (d_x, d_z) on Plane 1. This relationship can be expressed as

$$d_x = -t_x f_l / a \quad (3)$$
$$d_z = -t_z f_l / a$$

where f_l is the distance between the pinhole and the detector plane (focal length) and a is the distance between the pinhole and the plane parallel to the detector plane that includes the source point. The distance a can be expressed as

$$a = (h_x - x_1') \sin\theta + (h_y - y_1') \cos\theta \quad (4)$$

where $(h_x, h_y, h_z) = (r \sin\theta, r \cos\theta, 0)$ is the pinhole position translated by the rotation θ on the oblique circular orbit with radius of rotation r. We employed the MLEM[10,11] reconstruction algorithm for this pinhole geometry. The MLEM update for a two-orbit system can be expressed as

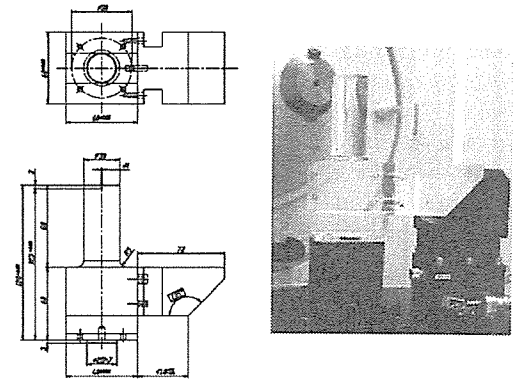

Fig. 3 Adjustment implement to position the point source at the COR of both orbits.

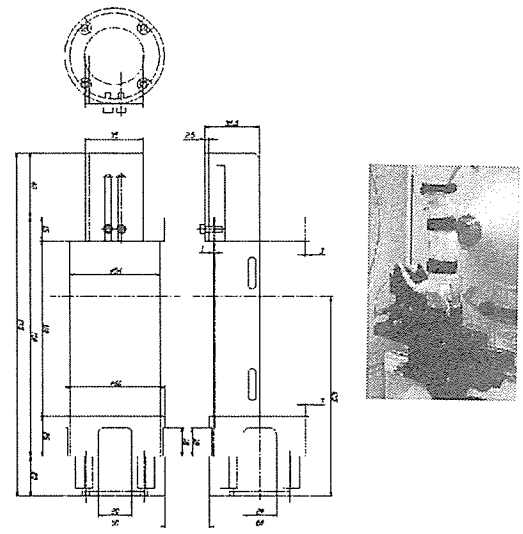

Fig. 4 Rat holder fabricated from 0.5 mm-thick vinyl chloride.

$$\lambda_j^{k+1} = \frac{\lambda_j^k}{\sum_{l=1}^{2}\sum_{i=1}^{n} c_{ij}} \sum_{l=1}^{2}\sum_{i=1}^{n} \frac{y_{li} c_{ij}}{\sum_{j=1}^{m} c_{ij}\,\lambda_j^k} \qquad (5)$$

where, as shown in Figure 5, λ_{jk} is the value of the image voxel j for the k-th iteration, y_{li} is the measured value of the projection pixel i for the l-th orbit, and c_{ij} is the probability of detecting a photon originating from image voxel j at projection pixel i for the l-th orbit.

Here, we used an OS scheme[12] to reduce the number of iterations. Subsets were evenly divided from both orbits for the OS scheme. A 3D voxel-driven projector using bilinear interpolation on the detector plane was employed in both forward- and back-projections. While back-projecting, the projection data from different orbits were transformed into the same coordinate and combined in the reconstructed 3D matrix space. The software was implemented on a 2.4-GHz PC with Xeon CPU and 1 GB of physical memory, running on a Linux operating system (version 2.4.18).

Experiment with a point source

In order to validate whether the projection data from two orbits were correctly acquired, we performed an experiment using a radioactive point source. A point source of about 1.4 mCi/ml of $^{99m}TcO_4^-$ was positioned at the COR using the adjustment implement (Fig. 3). A pinhole insert with a diameter of 4.8 mm was employed, and the distance between the pinhole center and point source was 39.5 mm. Projection data were acquired for 120 angular views in steps of 3°. The acquisition time for each step was 15 s. Three images were reconstructed from the projection data with the 90° orbit, 45° orbit, and both the orbits using the 3D OSEM algorithm (2 iterations and 8 subsets). The matrix size of the image was 128 × 128 × 128 and the voxel size was 0.76 × 0.76 × 0.76 mm^3 (zooming factor of 6.35).

Since the point source was positioned at the center of both the 90° and 45° orbits, its positions in the three images should be identical. The 3D position of the point source in each image was estimated by calculating the image center of gravity, and the estimated positions in the three images were compared.

Experiment with a line source

As described above, the misalignment of the COR could be problematic especially for two orbit data acquisition. Thus, in our system, the camera was kept fixed while the target object was rotated. For evaluating the misalignment of the COR for our system as well as the conventional system, experiments were performed using a line source phantom with an inner diameter of 1.14 mm. The phantom was filled with about 4.0 mCi of $^{99m}TcO_4^-$ solution. The phantom was carefully placed at the center in one projection view. First, the pinhole detector was rotated around the phantom with a rotation radius of 9 mm. Next, the phantom was rotated on the rotating stage. In both cases,

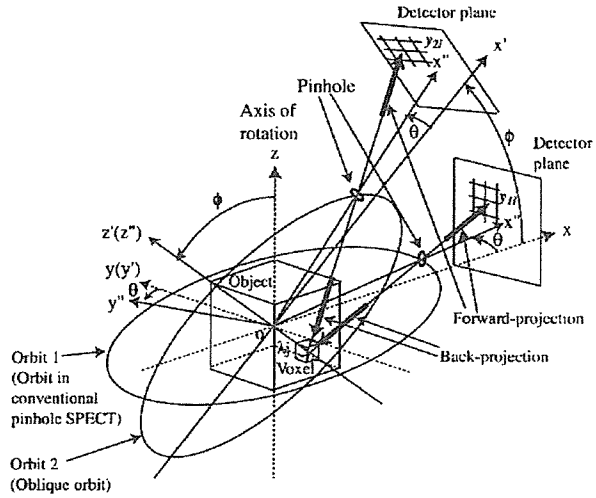

Fig. 5 Coordinate system of oblique circular orbits in pinhole SPECT with two circular orbits.

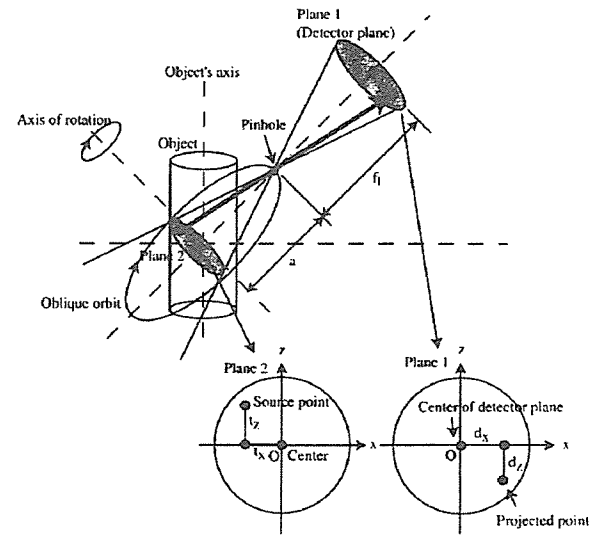

Fig. 6 Pinhole geometry for oblique orbit in pinhole SPECT with two circular orbits.

a pinhole with a diameter of 1 mm was used, and data were acquired from 120 angular views (3°/view). The data by both systems were reconstructed using the 3D OSEM algorithm.

Animal experiment

In order to demonstrate the reconstructed image by our system, a study was performed with a rat (SD rat; body weight: 150 g) and ^{99m}Tc-HMDP, an agent for bone scanning. ^{99m}Tc-HMDP was also accumulated in the bladder of the rat. Therefore, to eliminate the effect of radioactivity in the bladder, both kidneys of the rat were removed before ^{99m}Tc-HMDP (185 MBq/ml) was intra-

Table 1 Results of the experiment with a point source. Estimated position of the point source in the image

	x (mm)	y (mm)	z (mm)
90° orbit	0.0505	0.0511	0.0137
45° orbit	0.0464	0.0426	0.0290
both orbits	0.0643	0.0504	0.0165

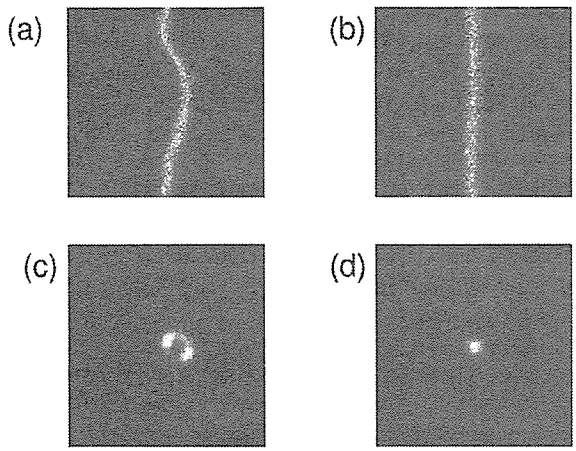

Fig. 7 Results of the experiments with the line source phantom. (a) Sinogram data measured by the conventional system (rotating the camera), (c) image reconstructed by the conventional system, (b) sinogram data measured by the proposed system (rotating the object), and (d) image reconstructed by the proposed system.

venously injected. The rat was set on the rotation unit of 90° orbit and data acquisition using the proposed system was begun 1 h after the injection. The rotation radius was 85 mm, and data were acquired from 120 angular views (3°/view) for 40 min. Subsequently, the rat was set on the rotation unit of the 45° orbit and data were acquired for 40 min. The energy window was 140 keV ± 10%. The diameter of the pinhole insert was 1 mm. The acquired data were sent to the PC for reconstruction using the 3D OSEM algorithm with two iterations and eight subsets. For comparison, the conventional filtered backprojection algorithm (the Feldkamp FBP algorithm)[9] was employed to reconstruct the image using the data acquired from the 90° orbit. No correction for attenuation of photons or scattered rays was made in any of the processes.

RESULTS

Experiment with a point source

Table 1 lists the estimated positions of the point source in the three reconstructed images. These three point-source positions were almost at the center (the distance from the center was 0.083 mm at maximum) and were close in value. This indicates a sufficient accuracy of intersection of the two axes and the pinhole center.

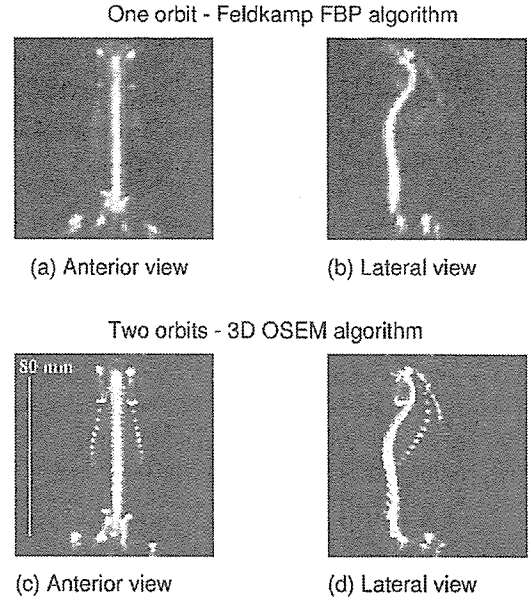

Fig. 8 Representative images of rat bone scintigrams by ^{99m}Tc-HMDP. The images of (a) and (b) were reconstructed using the Feldkamp FBP algorithm with data from the 90° orbit. The images of (c) and (d) were reconstructed using the 3D OSEM with two orbital data. All images were generated by the maximum intensity projection (MIP) method.

Experiment with a line source

Figure 7 shows the results of the experiments with a line source phantom. Misalignment of the COR was clearly observed when the camera was rotated. This results in an artifact on the reconstructed image (Fig. 7 (c)). On the other hand, no obvious artifact was observed when our system was used.

Animal experiment

Figure 8 shows the maximum intensity projection (MIP) images of the rat with ^{99m}Tc-HMDP obtained using the Feldkamp FBP algorithm with one set of orbital data and the 3D OSEM with two orbital data. The artifact of the image was significantly reduced, and a thin rib was clearly observed when data from two orbitals were used.

DISCUSSION

In this paper, we present the pinhole SPECT system for imaging small animals using data from two orbits. In the proposed system, the position of the detector is kept fixed while the target object is rotated.[22] As compared with the conventional system with one orbit, our system requires a more accurate adjustment of the COR. The experiments with the point and line sources indicated that our system achieved sufficient accuracy in adjusting the COR of the two orbits. This result was apparent in the bone scan with a rat. Image distortion and axial blurring observed in the

one orbital system were greatly improved in the proposed system with two orbits.

Metzler et al. proposed the use of a helical scan system in order to acquire complete data by pinhole SPECT.[23] In the helical scan, sensitivity may be hampered when the pinhole moves across the target object. On the other hand, the sensitivity of our system is not affected since the object is positioned at the center of the field-of-view.

The system proposed in this paper is still in the prototype stage, and in order to acquire data from two orbits, the object must be moved from one orbit to the other. We plan to build a system with multiple pinhole detectors in order to increase the sensitivity.

Our final goal is to develop a system that achieves quantitative functional imaging of small animals. Although the image quality achieved by the proposed system has dramatically improved, several issues have yet to be considered for quantification. Penetrated photons at the collimator and photons scattered from the object as well as the collimator will degrade the image quality and quantity.[24] It is also important to consider the sensitivity compensation of the pinhole collimator when reconstructing an image.[25] In order to achieve a quantitative functional image using the proposed system, these issues should be rectified in the future.

CONCLUSION

We developed a pinhole SPECT system for the imaging of small animals. The proposed system consists of two axes so that complete data are acquired. Image uniformity was dramatically improved by our system. This system will provide accurate quantitative information on the biological functions of small animals.

ACKNOWLEDGMENT

This study was financially supported by the Budget for Nuclear Research of the Ministry of Education, Culture, Sports, Science and Technology, based on screening and counseling by the Atomic Energy Commission.

REFERENCES

1. Chatziioannou AF. PET scanner dedicated to molecular imaging of small animal models. *Mol Imaging Biol* 2002; 4: 47–63.
2. Tai YC, Chatziioannou AF, Yang Y, Silverman RW, Meadors K, Siegle S, et al. MicroPET II: design, development and initial performance of an improved microPET scanner for small-animal imaging. *Phys Med Biol* 2003; 48: 1519–1537.
3. Jeavons AP, Chandler RA, Dettmar CAR. A 3D HIDAC-PET camera with submillimetre resolution for imaging small animals. *IEEE Trans Nucl Sci* 1999; 46: 468–473.
4. Weber DA, Ivanovic M, Franceschi D, Strand S-E, Erlandsson K, Franceschi M, et al. Pinhole SPECT: An approach to *in vivo* high resolution SPECT imaging in small laboratory animals. *J Nucl Med* 1994; 35: 342–348.
5. Jaszczak RJ, Li J, Wang H, Zalutsky MR, Coleman RE. Pinhole collimation for ultra-high-resolution small-field-of-view SPECT. *Phys Med Biol* 1994; 39: 425–437.
6. Ishizu, K, Mukai T, Yonekura Y, Pagani M, Fujita T, Magata Y, et al. Ultra-high resolution SPECT system using four pinhole collimators for small animal studies. *J Nucl Med* 1995; 36: 2282–2287.
7. Ogawa K, Kawade T, Nakamura K, Kubo A, Ichihara T. Ultra high resolution SPECT for small animal study. *IEEE Trans Nucl Sci* 1998; 45: 3122–3126.
8. Aoi T, Watabe T, Deloar HM, Ogawa M, Teramoto N, Kudomi N, et al. Absolute quantitation of regional myocardial blood flow of rats using dynamic pinhole SPECT. Conference Record of IEEE Nuclear Science and Medical Imaging Conference 2002.
9. Feldkamp LA, Davis LC, Kress JW. Practical cone beam algorithm. *J Opt Soc Am* 1984; 29: 612–619.
10. Shepp LA, Vardi Y. Maximum likelihood reconstruction for emission tomography. *IEEE Trans Med Imag* 1982; MI-1: 113–122.
11. Lange K, Carson R. EM reconstruction algorithms for emission and transmission tomography. *J Comput Assist Tomogr* 1984; 8: 306–316.
12. Hudson HM, Larkin RS. Accelerated image reconstruction using ordered subsets of projection data. *IEEE Trans Med Imag* 1994; 13: 601–609.
13. Vanhove C, Defrise M, Franken PR, Everaert H, Deconinck F, Bossuyt A. Interest of the ordered subsets expectation maximization (OS-EM) algorithm in pinhole single-photon emission tomography reconstruction: a phantom study. *Eur J Nucl Med* 2000; 27: 140–146.
14. Tuy HK. An inversion formula for cone-beam reconstruction. *SIAM J Appl Math* 1983; 43: 546–552.
15. Grangeat O, Sire P, Guillemaud R, La V. Indirect cone-beam three-dimensional image reconstruction. In: *Contemporary Perspectives in Three-Dimensional Biomedical Imaging*, Roux C, Coatrieux JL (eds), Amsterdam: IOS Press, 1997: 29–52, 343–350.
16. Kudo H, Saito T. Feasible cone beam scanning methods for exact reconstruction in three-dimensional tomography. *J Opt Soc Am A* 1990; 7: 2169–2181.
17. Kudo H, Saito T. Derivation and implementation of a cone-beam reconstruction algorithm for nonplanar orbits. *IEEE Trans Med Imag* 1994; 13: 196–211.
18. Kudo H, Saito T. An extended completeness condition for exact cone-beam reconstruction and its application. Conference Record of IEEE Nuclear Science and Medical Imaging Conference 1994, 1710–1714.
19. Zeniya T, Watabe H, Aoi T, Kim KM, Teramoto N, Hayashi T, et al. A new reconstruction strategy for image improvement in pinhole SPECT. *Eur J Nucl Med Mol Imag* 2004; 31: 1166–1172.
20. Li J, Jaszczak RJ, Greer KL, Coleman RE. A filtered backprojection algorithm for pinhole SPECT with a displaced center-of-rotation. *Phys Med Biol* 1994; 39: 165–176.
21. Li J, Jaszczak RJ, Coleman RE. Maximum likelihood reconstruction for pinhole SPECT with a displaced center-of-rotation. *IEEE Trans Med Imag* 1995; 14: 407–409.

22. Habraken JB, de Bruin K, Shehata M, Booij J, Bennink R, van Eck Smit BL, et al. Evaluation of high-resolution pinhole SPECT using a small rotating animal. *J Nucl Med* 2001; 42: 1863–1869.
23. Metzler SD, Greer KL, Jaszczak RJ. Helical pinhole SPECT for small-animal imaging: A method for addressing sampling completeness. *IEEE Trans Nucl Sci* 2003; 50: 1575–1583.
24. Deloar HM, Watabe H, Aoi T, Iida H. Evaluation of peneuration and scattering components in conventional pinhole SPECT: phantom studies using Monte Carlo simulation. *Phys Med Biol* 2003; 48: 1–14.
25. Smith MF, Jaszczak RJ. The effect of gamma ray penetration on angle-dependent sensitivity for pinhole collimation in nuclear medicine. *Med Phys* 1997; 24: 1701–1709.

Technical note

Nuclear Medicine Communications

Comparison of multi-ray and point-spread function based resolution recovery methods in pinhole SPECT reconstruction

Antti Sohlberg[a,b], Hiroshi Watabe[a], Tsutomu Zeniya[a] and Hidehiro Iida[a]

Background and objectives Statistical reconstruction methods allow resolution recovery in tomographic reconstruction. Even though resolution recovery has the potential to improve overall image quality, pinhole SPECT images are still often reconstructed using simplified models of the acquisition geometry in order to reduce reconstruction time. This paper investigates the benefits of two resolution recovery methods, multi-ray and point-spread function based, in pinhole SPECT by comparing them to uncorrected reconstruction.

Methods Resolution recovery was incorporated into ordered subsets expectation maximization reconstruction algorithm. The first of the correction methods used a simple but very fast multiple projection ray approach, whereas the second, much slower, method modelled the acquisition geometry more accurately using the analytical point-spread function of the pinhole collimator. Line source, Jaszczak and contrast phantom studies were performed and used for comparison.

Results Resolution recovery improved resolution, contrast and visual quality of the images when compared to reconstructions without it. The method based on the point-spread function performed slightly better, but was almost 50 times slower than the much simpler multi-ray approach.

Conclusion The multiple projection ray approach is a promising method for very fast and easy resolution recovery in pinhole SPECT. It has a profound effect on image quality and can markedly improve the resolution–sensitivity trade-off. *Nucl Med Commun* 27:823–827 © 2006 Lippincott Williams & Wilkins.

Nuclear Medicine Communications 2006, 27:823–827

Keywords: pinhole SPECT, resolution recovery, statistical reconstruction

[a]National Cardiovascular Center Research Institute, Suita City, Osaka, Japan and [b]Department of Clinical Physiology & Nuclear Medicine, Kuopio University Hospital, Finland.

Correspondence to Dr Antti Sohlberg, National Cardiovascular Center Research Institute, 5-7-1 Fujishiro-dai, Suita City, Osaka, Japan 565-8565.
Tel: +0081 6833 5012 (ext. 2559); fax: +0081 6 6835 5429;
e-mail: antti@ri.ncvc.go.jp

Received 13 February 2006 Accepted 4 May 2006

Introduction

The use of pinhole single photon emission computed tomography (SPECT) in clinical practice has been limited to small and superficial targets such as the thyroid [1] and joints [2] due to the reduced field of view. Recently, there has been renewed interest in pinhole SPECT, because it enables small animal imaging, where a small field of view is not a serious problem [3–7]. The attractiveness of small animal pinhole SPECT arises from the fact that it can be performed without any dedicated hardware using only a conventional gamma camera, whereas small animal PET, for example, requires an imaging device suitable only for laboratory animals [8].

The quality of SPECT is degraded by three main factors: attenuation, scatter and collimator blurring of which attenuation and scatter are less pronounced in small animal pinhole SPECT [9]. The collimator blurring reduces spatial resolution and forces the use of small diameter pinhole apertures at the cost of severely reduced sensitivity, which is the most important drawback of small animal pinhole SPECT. The sensitivity of pinhole SPECT can be increased by using multi-pinhole collimators [10], but this requires modifications to the standard clinical imaging equipment and is not widely applied. One solution to the poor sensitivity problem might be the use of statistical reconstruction methods such as the maximum likelihood expectation maximization (ML-EM) [11] or the ordered subsets expectation maximization (OS-EM) algorithms [12]. ML-EM and OS-EM can partly recover the loss in resolution caused by collimator blurring by incorporating a model of the acquisition geometry into the algorithm and might therefore allow the use of larger diameter pinhole apertures. Recovery of resolution has been shown to improve the quality of conventional SPECT imaging [13,14], but is not yet commonly used in small animal pinhole SPECT.

The biggest problem in incorporating resolution recovery in pinhole SPECT reconstruction is the large increase in computational burden. The calculation of point-spread function (PSF) look-up tables can take hours and might require several gigabytes of storage space. The fast resolution recovery methods such as the slice-to-slice blurring [15] often used in parallel-beam SPECT are not

0143-3636 © 2006 Lippincott Williams & Wilkins

very straightforward to extend for pinhole SPECT either due to converging nature of pinhole collimation. To overcome computational problems a relatively simple resolution recovery method for pinhole SPECT was recently presented [16]. This method is based on the use of multi-ray projections, where 7 or 21 projection rays, which intersect the pinhole aperture in a predetermined pattern, are used instead of a single ray going through the pinhole centre. The aim of this work is to compare the multi-ray projection approach to a method with a more accurate model of the acquisition geometry.

Materials and methods

Implementation of the algorithms

The ML-EM algorithm can be presented as

$$\lambda^{k+1}(b) = \frac{\lambda^k(b)}{\sum_d p(b,d)} \sum_d p(b,d) \frac{n^*(d)}{\sum_{b'} p(b',d)\lambda^k(b')} \quad (1)$$

where $\lambda(b)$ is the number of counts emitted from image voxel b, k is the number of iteration, $p(b,d)$ is the probability that the emission in voxel b is detected in detector bin d, and $n^*(d)$ is the measured projection count in detector bin d. The ML-EM algorithm updates the current image estimate using forward projection,

$$\sum_{b'} p(b',d)\lambda^k(b'),$$

and back-projection,

$$\sum_d p(b,d) \frac{n^*(d)}{\sum_{b'} p(b',d)\lambda^k(b')},$$

operations. In this study three different reconstruction algorithms based on ML-EM and accelerated using the ordered subsets approach were implemented. The first method (OS-EM_{noRR}) used a simple ray-driven forward projector/voxel-driven back-projector pair assuming zero pinhole diameter. The second algorithm (OS-EM_{rayRR}) was implemented using ray-driven forward projection with seven projection rays and voxel-driven back-projector with a single ray. The seven projection rays intersected the pinhole aperture in a hexagonal pattern modelling the effect of the finite pinhole aperture diameter by inverse cone of rays [16]. The third method (OS-EM_{psfRR}) incorporated analytical pinhole collimator point-spread functions into the reconstruction algorithm. The PSFs were calculated according to Metzler *et al.* [17] and stored into hard disk prior to reconstruction in contrast to approach used by the first and second method where the forward projection and back-projection were calculated on-the-fly during the reconstruction.

Phantom studies

The phantom studies were performed using a Toshiba GCA-7200A (Toshiba, Japan) gamma camera equipped with a 251 mm focal length pinhole collimator (0.5, 1.0 and 2.0 mm pinhole apertures specially fabricated for small animal studies). Three phantoms were imaged. The line source phantom consisted of a line source holder and single line source filled with 5 MBq of ^{99m}Tc and placed accurately on the axis of rotation. The resolution was measured as full width at half maximum of horizontal profile taken at the central slice of the phantom. The Jaszczak phantom had four sectors with 1.0, 1.5, 2.0 and 2.5 mm diameter rods separated by a distance twice the rod diameter (Fig. 1). The Jaszczak phantom was filled with 52 MBq of ^{99m}Tc and used to assess the image quality visually. The contrast phantom consisted of eight rods (2.0, 3.0, 4.0, 5.0, 6.0, 7.0, 8.0 and 9.0 mm diameter) and a large background compartment (Fig. 1). The rods were filled with an approximately five times higher concentration of ^{99m}Tc than the background. The total activity in the phantom was 780 MBq. The contrast for each rod was calculated as

$$C = \frac{I_{rod} - I_{bg}}{I_{rod} + I_{bg}} \quad (2)$$

Fig. 1

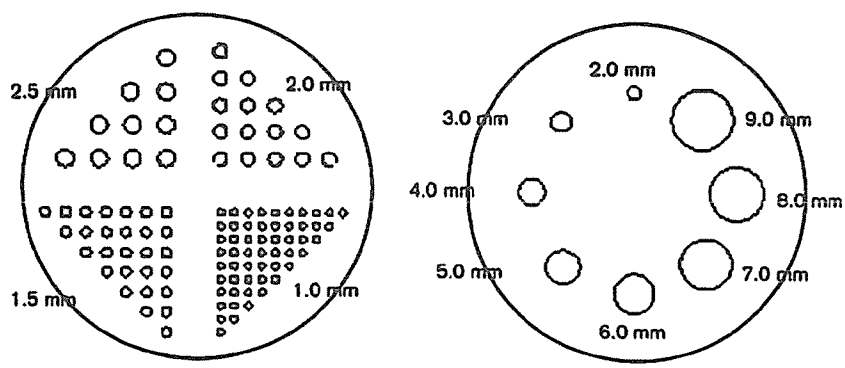

One slice of the Jaszczak phantom (on the left) and contrast phantom (on the right). The phantoms had outer diameter and height of 50 mm. The diameters of the rods are marked on the phantoms.

Table 1 Resolution (measured as full width at half maximum) for 0.5, 1.0 and 2.0 mm pinhole aperture diameters obtained from the line source phantom study, which was reconstructed using OS-EM (five iterations) with the three different resolution recovery methods: no resolution recovery (noRR), multi-ray based resolution recovery (rayRR) and point-spread function-based resolution recovery (psfRR)

	Aperture diameter (mm)		
Algorithm	0.5	1.0	2.0
noRR	1.4	1.6	2.4
rayRR	1.3	1.4	1.3
psfRR	1.2	1.4	1.3

where I_{rod} is the average count in the region of interest (ROI) of the rod and I_{bg} the average count in background ROI. The rod ROIs were circular and had the same diameter as the corresponding rod, whereas each background ROI was annular with inner diameter equal to the diameter of the rod and outer diameter was inner diameter plus 2 mm.

All the acquisitions were performed using 0.5, 1.0 and 2.0 mm pinhole aperture (60° opening angle), 55 mm radius of rotation, 4.3 mm pixel size (128 × 128 matrix), 360° circular orbit and 120 projection angles. In order to avoid centre of rotation shifts the projection data was acquired by rotating the target instead of the detector using the system presented by Zeniya *et al.* [18].

The imaging time per projection angle was selected so that the number of total projection counts was similar in the 0.5, 1.0 and 2.0 mm pinhole aperture studies. The average total projection counts in the line source, Jaszczak and contrast phantom study were 0.9 MCts, 5.2 MCts and 51.8 MCts. The images were reconstructed with the three OS-EM algorithms using eight subsets and five iterations with 0.94 mm voxel size.

Results

Table 1 presents the resolution values after five iterations for the three pinhole apertures and three algorithms. The resolution recovery clearly improves resolution and its effect is more pronounced at larger

Fig. 2

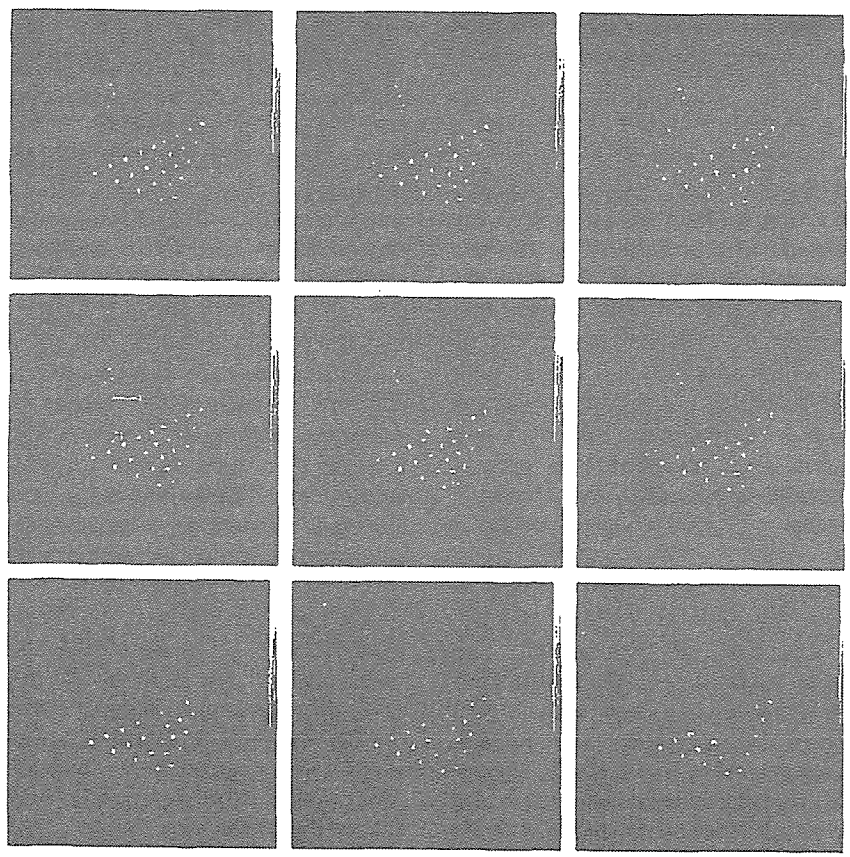

Transverse slices of the Jaszczak phantom study (five slices summed into one); from top to bottom 0.5, 1.0 and 2.0 mm pinhole aperture diameter and from left to right OS-EM with no resolution recovery, multi-ray based resolution recovery and point-spread function based resolution recovery. Air bubbles are marked with arrows on one of the images.

Table 2 **Contrast for 0.5, 1.0 and 2.0 mm pinhole aperture diameters obtained from the contrast phantom study reconstructed using OS-EM (five iterations) with the three different resolution recovery methods: no resolution recovery (noRR), multi-ray based resolution recovery (rayRR) and point-spread function based resolution recovery (psfRR)**

Rod diameter (mm)	Aperture diameter and resolution recovery method								
	0.5 mm			1.0 mm			2.0 mm		
	noRR	rayRR	psfRR	noRR	rayRR	psfRR	noRR	rayRR	psfRR
2.0	0.34	0.35	0.35	0.29	0.30	0.31	0.13	0.14	0.13
3.0	0.46	0.48	0.50	0.38	0.39	0.41	0.28	0.32	0.28
4.0	0.48	0.49	0.51	0.51	0.54	0.55	0.34	0.40	0.38
5.0	0.48	0.49	0.51	0.49	0.51	0.52	0.37	0.43	0.42
6.0	0.50	0.51	0.53	0.49	0.51	0.53	0.38	0.43	0.41
7.0	0.50	0.50	0.52	0.50	0.53	0.54	0.41	0.46	0.44
8.0	0.49	0.50	0.52	0.48	0.50	0.52	0.39	0.43	0.43
9.0	0.51	0.52	0.53	0.53	0.55	0.57	0.47	0.51	0.49

True contrast of the rods versus background according to Equation 2 is 0.67.

pinhole diameters. On the other hand, the results of the multi-ray and the point-spread function based methods do not differ much. The images of the Jaszczak phantom (Fig. 2) confirm the above findings. The resolution recovery has the biggest effect at the 2 mm pinhole diameter case and the quality of the OS-EM_{rayRR} and OS-EM_{psfRR} images is very similar. The results of the contrast phantom experiment after five iterations are illustrated in Table 2. The methods based on the point-spread function performs slightly better, overall, than does the multi-ray based method.

Discussion

This study compared fast multiple projection ray and analytical point-spread function based resolution recovery methods to uncorrected reconstruction in pinhole SPECT. The multi-ray and point-spread function approaches improved resolution and contrast. The greatest improvement in resolution and contrast was noticed at large pinhole diameters (Tables 1 and 2, Fig. 2). The poor performance of uncorrected reconstruction at larger pinhole diameters is due to the fact that at larger diameters the zero pinhole diameter assumption made in uncorrected reconstruction is violated more than at smaller aperture diameters.

As mentioned in the introduction the biggest problem in incorporating resolution recovery in pinhole SPECT reconstruction is the large computational burden. The calculation time for one iteration of the uncorrected pinhole OS-EM (1.7 GHz Intel processor with 1.0 GB RAM) was 4 min, whereas the computation time for OS-EM_{rayRR} and OS-EM_{psfRR} was 15 min and 10.5 h, respectively, using the acquisition parameters mentioned in the methods section. The reconstruction time of the PSF-based method includes the calculation of the system model, which dominates the calculation time. If the system model for the PSF-based resolution recovery is already stored in a hard disk prior to reconstruction the reconstruction procedure is very fast. Therefore the point-spread function based resolution recovery is suitable for systems where the imaging geometry is fixed [19], because every time the imaging geometry changes, a new system model needs to be generated. The OS-EM_{noRR} and OS-EM_{rayRR}, on the other hand, model the geometry during the reconstruction and can offer clinically acceptable reconstruction times in every case.

The resolution improvement achieved with resolution recovery is important because it allows the use of larger pinhole diameters, which provide higher sensitivity. The poor sensitivity of pinhole collimators has been the biggest problem in small animal pinhole SPECT. Several methods, such as multiple detector heads [3,20] and multiple pinholes [21], have been proposed to overcome this problem, but these approaches require either a multi-headed gamma camera and/or special hardware and are not yet widely applied. Larger injected activities or longer acquisition times are not an optimal approach either, because the radiation burden to the animal or the difficulty of maintaining proper anaesthesia can cause problems. Resolution recovery with a fast resolution recovery algorithm, on the other hand, is almost free of side effects. The only drawback of the multi-ray based approach method is a small increase in noise when compared to reconstruction without resolution recovery, which has been illustrated by Beque *et al.* [16]. The coefficient of variation (COV = standard deviation/mean × 100%) of a large ROI drawn on the uniform background of the contrast phantom also showed this small noise increase. After five iterations the COVs for the 0.5 mm pinhole aperture diameter were 16.1%, 15.4 and 13.7%, when reconstructed with OS-EM_{noRR}, OS-EM_{rayRR} and OS-EM_{psfRR}. The respective values for the 1.0 mm aperture were 16.7%, 17.0% and 14.0%, and 14.6%, 15.9% and 8.4% for the 2.0 mm aperture. The noise properties of the resolution recovery methods were not investigated in detail in this study, because they depended on the implementation of the algorithms. For instance, the noise level of the multi-ray based method

could be decreased by implementing resolution recovery also in the back-projector, but unfortunately this happens at the expense of increased computation time. Noise can also be decreased by using Bayesian reconstruction methods [7], which are almost as fast to execute as the common OS-EM. Therefore from the point of view of the computational burden the best alternative for noise reduction when multi-ray resolution recovery is applied might be to use Bayesian reconstruction methods and model collimator blurring only into the forward projector.

Even though the results presented in this paper were obtained from phantom experiments with activity levels higher than normal can be found in target organs in small animal studies, we are confident that the resolution recovery offers similar improvement in resolution and contrast in small animal studies. However, it is difficult to predict what kind of impact these improvements have, e.g. in brain receptor quantification or measurement of myocardial infarct size in mice and rats. Therefore we plan to further investigate the effect of resolution recovery on (semi-) quantitative values in most frequently used small animal models.

Conclusion

The fast multi-ray resolution recovery method performs almost as well as resolution recovery with accurate point-spread functions and therefore shows promise in improving the resolution–sensitivity trade-off in small animal pinhole SPECT.

Acknowledgement

This work was supported by Japan Society for the Promotion of Science and Nuclear Diagnostics AB.

References

1 Wanet PM, Sand A, Abramovici J. Physical and clinical evaluation of high-resolution thyroid pinhole tomography. *J Nucl Med* 1996; 37:2017–2020.
2 Bahk YW, Chung SK, Park YH, Kim SH, Lee HK. Pinhole SPECT imaging in normal and morbid ankles. *J Nucl Med* 1998; 39:130–136.
3 Acton PD, Choi SR, Plossl K, Kung HF. Quantification of dopamine transporters in the mouse brain using ultra-high resolution single-photon emission tomography. *Eur J Nucl Med Mol Imaging* 2002; 29:691–698.
4 Booij J, de Bruin K, Habraken JBA, Voorn P. Imaging of dopamine transporters in rats using high-resolution pinhole single-photon emission tomography. *Eur J Nucl Med Mol Imaging* 2002; 29:1221–1224.
5 Habraken JBA, de Bruin K, Shehata M, Booij J, Bennink R, van Eck Smit BLF, Busemann Sokole E. Evaluation of high-resolution pinhole SPECT using a small rotating animal. *J Nucl Med* 2001; 42:1863–1869.
6 Scherfler C, Donnemiller E, Schocke M, Dierkes K, Decristoforo C, Oberladstatter M, *et al.* Evaluation of striatal dopamine transporter function in rats by *in vivo* beta-[^{123}I]CIT pinhole SPECT. *Neuroimage* 2002; 17:128–141.
7 Sohlberg A, Lensu S, Jolkkonen J, Tuomisto L, Ruotsalainen U, Kuikka JT. Improving the quality of small animal brain pinhole SPECT imaging by Bayesian reconstruction. *Eur J Nucl Med Mol Imaging* 2004; 31:986–994.
8 Chatziioannou AF. Molecular imaging of small animals with dedicated PET tomographs. *Eur J Nucl Med Mol Imaging* 2002; 29:98–114.
9 Meikle SR, Kench P, Kassiou M, Banati RB. Small animal SPECT and its place in the matrix of molecular imaging technologies. *Phys Med Biol* 2005; 50:R45–R61.
10 Schramm NU, Ebel G, Engeland U, Schurrat T, Béhé M, Behr TM. High-resolution SPECT using multipinhole collimation. *IEEE Trans Nucl Sci* 2003; 50:315–320.
11 Shepp LA, Vardi Y. Maximum likelihood reconstruction for emission tomography. *IEEE Trans Med Imag* 1982; MI-1:113–122.
12 Hudson HM, Larkin RS. Accelerated image reconstruction using ordered subsets of projection data. *IEEE Trans Med Imag* 1994; 13:601–609.
13 Hutton BF, Lau YH. Application of distance-dependent resolution compensation and post-reconstruction filtering for myocardial SPECT. *Phys Med Biol* 1998; 43:1679–1693.
14 Yokoi T, Shinohara H, Onishi H. Performance evaluation of OSEM reconstruction algorithm incorporating three-dimensional distance-dependent resolution compensation for brain SPECT: a simulation study. *Ann Nucl Med* 2002; 16:11–18.
15 Zeng GL, Bai C, Gullberg GT. A projector/backprojector with slice-to-slice blurring for efficient three-dimensional scatter modeling. *IEEE Trans Med Imaging* 1999; 18:722–732.
16 Beque D, Vanhove C, Andreyev A, Nuyts J, Defrise M. *Correction for Imperfect Camera Motion and Resolution Recovery in Pinhole SPECT.* IEEE Nuclear science symposium and medical imaging conference rome, Italy 2004.
17 Metzler SD, Bowsher JE, Greer KL, Jaszczak RJ. Analytic determination of the pinhole collimator's point-spread function and RMS resolution with penetration. *IEEE Trans Med Imag* 2002; 21:878–887.
18 Zeniya T, Watabe H, Aoi T, Kim KM, Teramoto N, Hayashi T, *et al.* A new reconstruction strategy for image improvement in pinhole SPECT. *Eur J Nucl Med Mol Imaging* 2004; 31:1166–1172.
19 Beekman FJ, Vastenhouw B. Design and simulation of a high-resolution stationary SPECT system for small animals. *Phys Med Biol* 2004; 49: 4759–4792.
20 Ishizu K, Mukai T, Yonekura Y, Pagani M, Fujita T, Magata Y, *et al.* Ultra-high resolution SPECT system using four pinhole collimators for small animal studies. *J Nucl Med* 1995; 36:2282–2287.
21 Beekman FJ, van der Have F, Vastenhouw B, van der Linden AJ, van Rijk PP, Burbach JP, *et al.* U-SPECT-I: a novel system for submillimeter-resolution tomography with radiolabeled molecules in mice. *J Nucl Med* 2005; 46:1194–1200.

ELSEVIER

NeuroImage

www.elsevier.com/locate/ynimg
NeuroImage 33 (2006) 1126–1135

Quantitative mapping of basal and vasareactive cerebral blood flow using split-dose ^{123}I-iodoamphetamine and single photon emission computed tomography

Kyeong Min Kim,[a,f] Hiroshi Watabe,[a] Takuya Hayashi,[a] Kohei Hayashida,[b] Tetsuro Katafuchi,[b] Naoyuki Enomoto,[b] Toshiyuki Ogura,[c] Miho Shidahara,[a] Shugo Takikawa,[c] Stefan Eberl,[d] Mayumi Nakazawa,[e] and Hidehiro Iida[a,*]

[a]*Department of Investigative Radiology, National Cardiovascular Center Research Institute, 5-7-1 Fujishiro-dai, Suita City, Osaka, 565-8565, Japan*
[b]*Department of Radiology, National Cardiovascular Center Hospital, Osaka, Japan*
[c]*Department of Neurosurgery, Azabu Neurosurgery Hospital, Sapporo City, Japan*
[d]*Department of Nuclear Medicine, Royal Prince Alfred Hospital, Sydney, Australia*
[e]*Nihon Medi-Physics, Tokyo, Japan*
[f]*Nuclear Medicine Laboratory, Korea Institute of Radiological and Medical Sciences, Seoul, Korea*

Received 17 October 2005; revised 1 March 2006; accepted 25 June 2006
Available online 10 October 2006

A new method has been developed for diffusible tracers, to quantify CBF at rest and after pharmacological stress from a single session of dynamic scans with dual bolus administration of a radiotracer.

The calculation process consisted of three steps, including the procedures of incorporating background radioactivity contaminated from the previous scan. Feasibility of this approach was tested on clinical SPECT studies on 16 subjects. Two sequential SPECT scans, 30 min apart, were carried out on each subject, after each of two split-dose administrations of 111 MBq IMP. Of these, 11 subjects received acetazolamide at 10 min before the second IMP injection. Additional PET scans were also carried out on 6 subjects on a separate day, at rest and after acetazolamide administration. The other 5 subjects were scanned only at rest during the whole study period.

Quantitative CBF obtained by this method was in a good agreement with those determined with PET (y(ml/100 g/min) = 1.07 × (ml/100 g/min) − 1.14, r = 0.94). Vasareactivity was approximately 40% over the whole cerebral area on healthy controls, which was consistent with a literature value. Reproducibility of CBF determined in the rest–rest study was 1.5 ± 5.7%. Noise enhancement of CBF images, particularly the second CBF, was reduced, providing reasonable image quality.

Repeat assessment of quantitative CBF from a single session of scans with split-dose IMP is accurate, and may be applied to clinical research for assessing vascular reactivity in patients with chronic cerebral vascular disease.

© 2006 Elsevier Inc. All rights reserved.

Keywords: Split-dose administration; ^{123}I-IMP SPECT; CBF mapping

Introduction

Positron emission tomography (PET) and single photon emission computed tomography (SPECT) are capable of providing physiological functions *in vivo* in a quantitative manner. This is based on mathematical modeling of the kinetic behavior in the body of a tracer that highlights the physiological processes of interest. Two important assumptions are often made, namely, (a) the physiological functions measured are constant over the whole study period, and (b) there is no residual tracer in the body before the tracer administration. These requirements give rise to a crucial restriction in the detection of temporal change of physiological parameters such as cerebral blood flow (CBF). Only a single set of parameters can be determined for a given physiological condition from a series of PET or SPECT measurements. In case of additional assessment at a different physiological condition, an additional scan has to be initiated after decay or excretion of the radioactivity from the body, and the stimulation needs to be applied before the next scan.

One advantage of tracer with a short-lived radioisotope such as ^{15}O in PET is that the radioactivity decays quickly (approximately 2 min half life), which allows a repeat assessment of CBF for several condition within a reasonable interval of typically 10–15 min. However, most PET tracers with longer half-lived radioisotope, such as ^{18}F and ^{11}C, and most SPECT tracers, require background radioactivity compensation, which may be obtained by using the first scan as background or performing an additional image immediately before the second tracer injection. This background subtraction method has been applied to many perfusion studies with SPECT (Hashikawa et al., 1994; Oku et al., 1994; Hattori et al., 1996; Imaizumi et al., 2002), and even to $H_2^{15}O$

* Corresponding author. Fax: +81 6 6835 5429.
E-mail address: iida@ri.ncvc.go.jp (H. Iida).
Available online on ScienceDirect (www.sciencedirect.com).

1053-8119/$ - see front matter © 2006 Elsevier Inc. All rights reserved.
doi:10.1016/j.neuroimage.2006.06.064

PET studies (Chmielowska et al., 1998; Chmielowska et al., 1999). The subtraction method, however, degrades the image quality and quantitative accuracy. A tracer that shows clearance or limited retention in the tissue requires minimizing the scan period for the background not to affect the parameter estimation in the second scan, but this results in the degraded image quality. In turn, a prolongation of the background scan, intended to prevent degrading image quality, causes inconsistency with the parameter estimation due to the time-dependent distribution of the tracer in the next. Clearance of the tracer from tissue is observed not only in the PET study using $H_2^{15}O$ but also in several SPECT studies, such as ^{123}I-iodoamphetamine (IMP) for quantitation of CBF (Iida et al., 1994a,b).

For repeat CBF studies in a single session, we have presented a new mathematical formulation to compensate for the background radioactivity contamination in tissue from the tracer previously administered (Iida et al., 2000; Nishizawa et al., 2003). This allows estimation of "snapshot"-like background radioactivity distribution just before the second tracer scan from the information obtained from whole the previous scan data assuming a compartment model. This background distribution was then built into a model for the parameter estimation using the second tracer data. Based on this formulation, we demonstrated the applicability of this approach to repeat CBF measurement using $H_2^{15}O$ PET in a shorter interval (Watabe et al., 2002).

In this study, we have aimed to make the CBF images of repeat SPECT scan, based on the above formulation, and to evaluate the validity and applicability of this functional mapping method by means of clinical studies performed with SPECT and IMP. Quantitative accuracy of this method was also tested by comparing CBF values with those in $H_2^{15}O$ PET studies.

Materials and methods

Theory

The new mathematical approach, Dual-Table autoradiography (ARG) method was formulated for a cerebral perfusion tracer, which has high trans-capillary extraction to the cerebral tissue with significant clearance. IMP has been chosen in this study. It was assumed that the kinetics of this tracer follows a single-tissue compartment model (Kuhl et al., 1982; Iida et al., 1994a, b). The calculation of CBF at baseline and after the pharmacological stress included three processes as shown in Fig. 1. The first process calculates a CBF (f_1) map from an early image obtained immediately after the first tracer administration based on a previously validated *in vivo* autoradiography technique for IMP, by employing a lookup table procedure (Fig. 1A) (Iida et al., 1994a,b; Iida et al., 1996). The second process estimates a background radioactivity distribution immediately before the next injection of IMP, using the CBF image obtained from the first process (Fig. 1B). This is an inverse procedure of the first process, but estimates the momentary ("snapshot"-like) radioactivity distribution at the time of the second IMP injection. The third process then calculates a CBF (f_2) map after the pharmacological stress from the next early image in addition to the background image generated by the second process (Fig. 1C). For this calculation, the tissue radioactivity concentration was formulated as follows:

$$\int_{T_1}^{T_2} C_t(t)\mathrm{d}t = f_2 \cdot \int_{T_1}^{T_2} C_a(t) \otimes e^{-\frac{f_2}{V_d}t}\mathrm{d}t + C_t\left(T^{\mathrm{bkg}}\right) \cdot \int_{T_1}^{T_2} e^{-\frac{f_2}{V_d}(t-T^{\mathrm{bkg}})}\mathrm{d}t \qquad (1)$$

where $C_t(t)$ is regional tissue radioactivity concentration (cps/g) in the next early image at time t, f_2 CBF (ml min/g) after the pharmacological stress, V_d distribution volume of the tracer (ml/ml), T_1 and T_2 the scan start and end times for the second scan, respectively, T^{bkg} is the time defined for the background activity before T_1, $C_a(t)$ arterial input function (cps/g), and $\otimes$ convolution integral, respectively. The first-pass extraction fraction is assumed to be unity and independent of time.

The lookup table process therefore includes two tables (see Fig. 2), namely response to the second tracer administration (the first term in the right of Eq. (1)) and the contribution of remaining radioactivity (the second term in the right of Eq. (1)). The second table is scaled by the background counts, $C_t(T^{\mathrm{bkg}})$

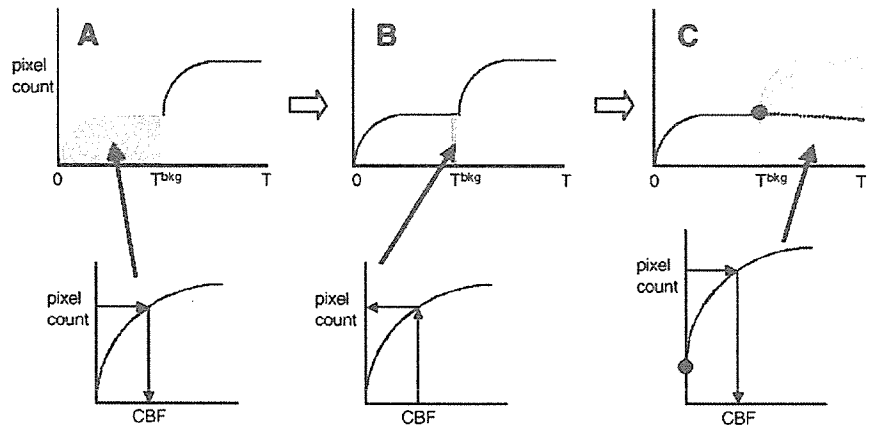

Fig. 1. Mathematical procedure to estimate the first and second CBF maps from a series of SPECT scans following split-dose administration of IMP. The calculation process consists of three steps, namely, (A) calculation of a baseline CBF map from the early image according to the IMP autoradiography, (B) estimation of a transient radioactivity distribution at the end of the scan (or at the time of the next scan initiation) from the CBF map, and (C) calculation of additional CBF map from the second SPECT image. Note that the estimated background distribution is implemented in the model formulation of the second CBF calculation process. Pharmacological stress can be given prior to the second IMP administration in a typical clinical study.

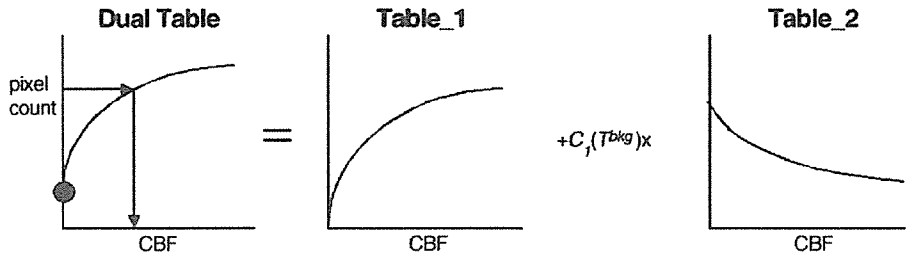

Fig. 2. The procedure to estimate the CBF map from the second SPECT scan. Once a table between CBF and SPECT counts is generated, a lookup table procedure provides a CBF map from pixel counts of the second SPECT image. This table is the sum of two tables corresponding to each term of Eq. (1). The first component corresponds to the response to the newly supplied tracer, and the second table corresponds to the contribution of background activity. Note that the second table is scaled in each pixel by referring the background radioactivity counts at the time of the second scan initiation, which are generated from the previous CBF map.

It is likely that CBF varies during the scan, particularly when pharmacological challenge is given before the end of the first scan. With the definition of a transient weight function, $w(t)$, describing effects of the transient CBF change on the estimated background radioactivity that should be used in the next CBF calculation, the observed tissue concentration, $C_i(T)$, is expressed with $w(t)$ and the transient CBF or $f(t)$ as (Iida et al., 1991);

$$C_i(T) = \int_0^T w(t) f(t) \mathrm{d}t \tag{2}$$

With assuming a two-compartment model for a constant f during the study and differentiation, $w(t)$ can be approximated by:

$$w(t) \approx \frac{\mathrm{d}C_i(t)}{\mathrm{d}t} \tag{3}$$

Thus the transient weight in the estimated background image is nearly equal to the first derivative of the tissue concentration curve during the previous scan. This suggests that the estimated background distribution for the next scan is predominantly sensitive to flow during the rising period following the bolus injection of IMP, and is only moderately affected by flow after a certain period has elapsed from the previous scan. Thus, minimal effects are expected in the background estimation process, even when pharmacological stress is applied before end of the previous scan.

Subject

Studies were performed on subjects. Subjects were divided into 3 groups. The first group ($n=5$) was consisted of clinical patients with cerebral ischemia, who were assigned to the IMP SPECT studies for clinical diagnosis, and were used to evaluate the reproducibility of the method. In this group, patients were scanned at rest during the whole study period (rest–rest condition). Their age ranged from 51 to 71 years old (mean±SD; 61±9). Four patients suffered from chronic cerebral hemorrhage, and one had an unruptured aneurysm.

The second group consisted of only healthy male volunteers ($n=5$), who had no signs or symptoms of stroke or other ischemic diseases, and were expected to show normal range of CBF values. All subjects belonging to this group were studied at rest during the first scan, but acetazolamide (ACZ) was administrated before the second IMP injection (rest-ACZ condition). Their ages ranged from 27 to 35 (mean±SD; 30±4).

The third group included 6 patients with stenosis or occlusion of extracranial internal carotid artery on unilateral ($n=3$) or bilateral ($n=3$) side. Their age ranged from 71 to 74 years old (mean±SD; 72±1). All patients underwent the IMP SPECT scans at rest and with an acetazolamide challenge, as in the second group, and PET scans following intravenous ^{15}O–water both at rest and after the same dose of acetazolamide, were done 2 days apart from the SPECT study with acetazolamide challenge. The second scan data of one subject among the subjects in this group, were excluded in the data analysis, because of the severe head motion and urination during SPECT acquisition.

All subjects had MRI scans prior to the SPECT study, which has been used for identification of region-of-interest (ROI) and also for generating attenuation maps that have been utilized for corrections of attenuation and scatter in the SPECT reconstruction (see below). All subjects gave written informed consent, and were studied by the protocol approved by the local ethical committee.

SPECT scan

All SPECT studies were carried out following the split-dose administration of IMP. For the first and the second groups, a triple-headed SPECT camera attached with low-energy high-resolution fan-beam collimator (GCA-9300A, Toshiba Medical System, Tokyo, Japan), installed at Azabu Neurosurgery Hospital, was used. And a dual-headed gamma camera attached with low-energy high-resolution fan-beam collimator (ECAM, Siemens Medical System, USA), installed at National Cardiovascular Center Hospital was used for the third group. The size of acquired projection was 64-by-64 pixels, and the energy window selected was 20% on the center of 159 keV for all studies.

In each subject, the split-dose IMP injections (111 MBq each) were separated by an interval of 30 min. The infusion period was 1 min, and was controlled using a constant infusion pump (Terumo, Tokyo, Japan). Two sets of dynamic SPECT scans were initiated at the time of the IMP injection. The duration of each dynamic scan was 30 min for the 1st and 2nd groups and 25 min for the 3rd group, respectively. For both SPECT scans, the detectors were rotated continuously collecting 60 projections over 360° initially every 10 s and, after 5 min, every 2 min for the triple-headed camera, and initially every 2 min and, after 10 min, every 5 min for the dual-headed camera. The acquired projection data

were re-binned to parallel beam projection for further process. Each dynamic projection data with the parallel-beam transformation were summed to a static data for each session, and two sets of images were reconstructed for further image calculation (see below). In the second and third groups, 16 mg/kg (1000 mg maximum) of acetazolamide was administered intravenously at 20 min after the first IMP injection.

Arterial input function was determined in individual studies. Arterial blood was sampled from the radial artery at 15-s intervals during the first 2 min with gradual prolongation thereafter. The whole blood radioactivity concentration was counted using a well counter, and its octanol extraction fraction was also counted as reported previously (Kuhl et al., 1982; Lear et al., 1982; Kurisu et al., 2002).

A uniform cylindrical phantom of 16-cm diameter (axial length of 15 cm) filled with approximately 20 MBq of ^{123}I-solution was scanned following the same scan protocol as for the clinical SPECT studies. The solution was sampled and its radioactivity concentration was counted in the well counter that was used for measuring the arterial blood radioactivity concentration.

PET scan

Six subjects belonging to the third group underwent a series of PET scans within 2-day period from the IMP study. The ECAT Exact47 PET scanner (Siemens-CTI Inc., Knoxville, USA) was used, which provides 47 tomographic slices. The observed spatial resolution of reconstructed image was approximately 7-mm FWHM both in-plane and in axial direction.

After a transmission scan for attenuation correction, a 90-s scan was performed following a bolus injection of ^{15}O-labeled water ($H_2^{15}O$). The functional CBF images were calculated according to the $H_2^{15}O$ autoradiography (ARG) technique (Kanno et al., 1987). The partition coefficient of water was assumed to be 0.80 ml/g, which was meant to minimize effects of tissue heterogeneity (Iida et al., 1988). The arterial input function was determined from the continuously monitored arterial blood time–activity curve including corrections for delay and dispersion (Iida et al., 1986, 1989). The scans were performed twice, the first at rest, and the second at 10 min after administration of the same dose of acetazolamide as in the SPECT study.

SPECT image reconstruction

To generate uniform attenuation map by means of MRI image, both static projections of the first and second sessions were reconstructed without correction of attenuation or scatter, to provide SPECT images for each session, and MRI image of each subject was co-registered to the reconstructed image without attenuation correction, using SPM2 (Welcome Department of Imaging Neuroscience, University College London, London, UK). The co-registered MRI image was converted to an attenuation map, after defining the head contour and assigning a value of uniform attenuation coefficient of 0.167 cm^{-1} into the area inside the head contour (Iida et al., 1998). The uniform attenuation map was used in image reconstruction with corrections of attenuation and scatter. Scatter component in emission projection was corrected by employing a technique of transmission-dependent convolution subtraction (TDCS), as previously validated (Meikle et al., 1994; Narita et al., 1996; Iida et al., 1998). The TDCS can provide the pixel-by-pixel estimation, $k(x, y)$, of scatter component in measured emission data, by means of the following formulation:

$$k(x,y) = 1 \frac{1}{A - B \cdot t(x,y)^{\beta/2}} + k_0 \quad (4)$$

where $t(x, y)$ is an attenuation factor for pixel (x, y) and k_0 is a term illustrating both septal penetration and scatter in the collimator due to contamination of high-energy photon of ^{123}I. The parameter sets for TDCS are $A=2.4718$, $B=A-1$, $\beta=0.2088$, and $k_0=0.2141$ for the triple-headed camera, $A=2.3069$, $B=A-1$, $\beta=0.2926$, and $k_0=0.3000$ for the dual-headed camera, respectively. These parameters were empirically determined by the previous study (Kim et al., 2001). The scatter-corrected projections were then reconstructed using the in-house package for quantitative SPECT reconstruction (QSPECT), which employed the ordered-subset expectation maximization (OS-EM) algorithm including the attenuation correction with the attenuation map (Hudson and Larkin, 1994). The reconstructed images were then cross-calibrated to the well counter system using the cross-calibration factor determined as below.

Images of the cylindrical phantom were reconstructed following the same procedures as for the clinical study, including correction for scatter and attenuation. A circular region-of-interest (ROI) of 8-cm diameter was placed on the transverse image, and mean counts over this ROI were referred to the radioactivity concentration of this solution (cps/g) measured by the well counter. The ratio of these two values was defined as the cross-calibration factor between the SPECT and the well counter system.

Data analysis

The reconstructed images of the first and second session were realigned using SPM2, to correct a possible head motion between both scan sessions. Quantitative CBF images were calculated for both the first and second SPECT images, respectively, as described in the theory, with setting T^{bkg} to T_1. The distribution volume of IMP, V'_d, was fixed at 35 ml/ml in the CBF calculation (Hatazawa et al., 1997; Iida et al., 1998). The image of background radioactivity generated during CBF calculation was compared with the reconstructed image immediately before the second IMP injection, i.e., the image with scan duration of 20–30 min for the first and second groups, and 20–25 min for the third group, respectively. All calculated CBF images of SPECT and PET were co-registered to its own MRI image, using SPM2.

In total, 39 circular ROIs with 2 cm of diameter were placed on MRI image, to cover the whole brain according to the criteria described elsewhere (Yamaguchi et al., 1986; Iida et al., 1998). These ROIs were projected on all CBF images to investigate the reproducibility between the first and second scans, and the consistency of the proposed method with PET. The rest–rest study was used to evaluate the reproducibility of the estimated CBF values between the two sessions, while the rest–acetazolamide study was used to evaluate the vasareactivity in normal subjects (namely the second group). Consistency of the calculated CBF values between the present method and PET was also evaluated.

All data were presented as mean ± SD, and Pearson's correlation and linear regression analysis were used to evaluate relationships between the two CBF values. The reproducibility of both measured and estimated background images was evaluated by means of Mann–Whitney rank sum test.

Results

Figs. 3A–C show a comparison of the background radioactivity concentration at 25 min after the first IMP injection estimated by the present model-based approach, with those obtained from a scan with short duration. Fig. 3A is a typical comparison of the background images obtained from one study among the first group. It appears that the estimated images show visually smoother, therefore smaller noise, than the measured images, while the absolute counts are equivalent. ROI counts of the estimated background images were also compared with those of the measured images for the rest–rest studies of the 1st group and the rest–acetazolamide studies of the third group in Figs. 3B and C, respectively. There is no significant difference between the two methods both in the rest–rest ($p>0.5$) and rest–acetazolamide ($p>0.1$) studies. However, the rest–acetazolamide study indicated slightly greater spread about the regression line.

Fig. 4A shows comparison of CBF images obtained from one of the rest–rest studies, indicating the reproducibility of the CBF measurement by the present method (Dual-Table ARG method). The visual difference between the estimated and measured background images in Fig. 3A leaded to the similar quality between the first and second CBF image set, although there is some difference in noise between test and retest. It is clear that the quantitative values of CBF are consistent between the two CBF images obtained from the first and second scans (see also Fig. 4B). The reproducibility between the two CBF values obtained from the rest–rest study as evaluated as a deviation of the two averages between the first and second CBF values was 1.5±5.7%. There was no significant difference between them.

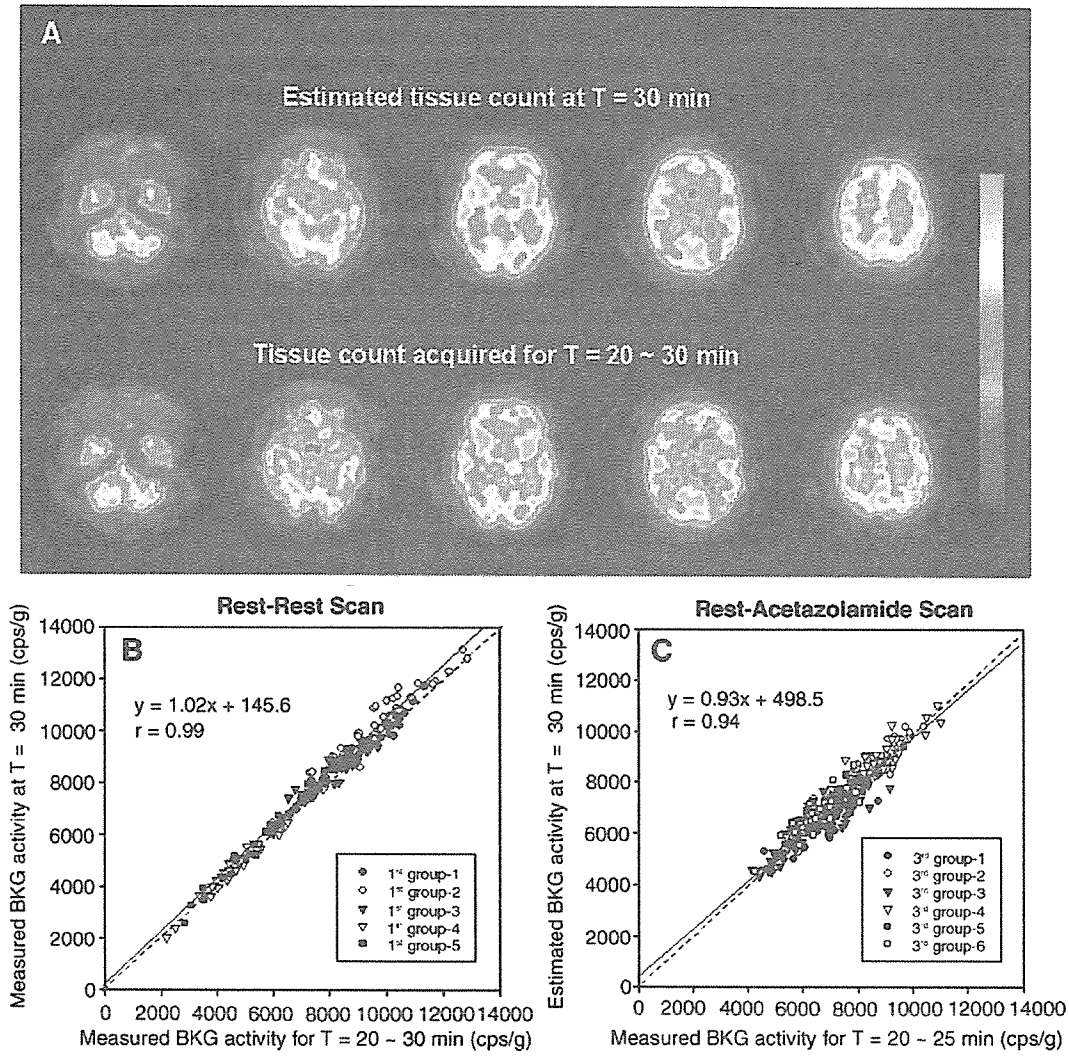

Fig. 3 (A) Comparison of background images estimated by the proposed method (top) with those acquired by a 10-min scan (t 20 30 min) with the triple-headed camera. (B) Comparison of pixel counts estimated by the proposed method with those acquired by a 10-min scan with the triple-headed camera. Values were obtained from 39 circular regions of interest that had a size of 314 mm^2. Data are obtained from the rest rest studies (n 5), and regression lines are plotted for each subject. (C) Same as for panel (B) but from the rest acetazolamide studies, in which background activity was compared with those by a 5-min scan (t 20 25 min) with dual-headed camera.

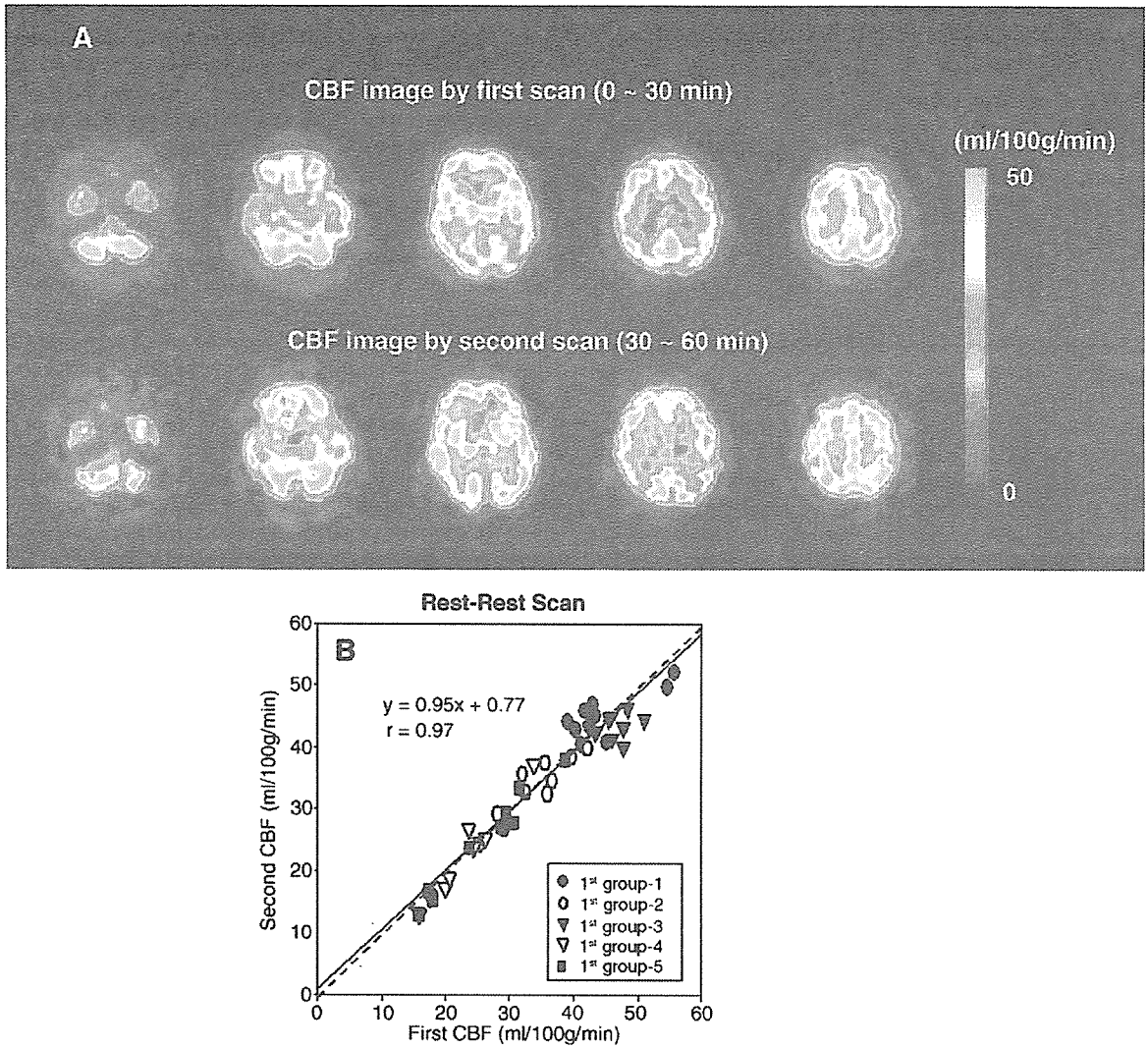

Fig. 4. (A) A comparison of calculated CBF images obtained from a typical clinical study with the rest–rest protocol. CBF images are shown for both first (top) and second (bottom) scans, demonstrating reproducibility of the method. All images are displayed with the same color scale in units of ml/100 g/min. (B) Comparison of calculated CBF values obtained from the rest–rest studies ($n=5$). Each value corresponds to a mean value of regions of interest in each area of deep and cortical gray matter (frontal, temporal, occipital gyri) and cerebellum. No significant difference was observed between the first and the second CBF values.

In the second group, CBF values of three gray matter regions (e.g., cortical and deep gray matter and cerebellum) were 37.4 ml/100 g/min, 36.4 ml/100 g min, and 44.4 ml/100 g/min for rest state, and 53.1 ml/100 g/min, 51.5 ml/100 g/min, and 63.7 ml/100 g/min for acetazolamide state, respectively (Figs. 5A, B). The CBF values of whole region including white matter, which were obtained from the 39 ROIs, were 37.1 ± 5.0 ml/100 g/min for rest and 52.2 ± 8.0 ml/100 g/min for acetazolamide states, respectively. These CBF values resulted in the global CBF increase of 40.5 ± 9.4%, and was homogeneous in all cerebral regions (43.0% for cortical, 42.3% for deep gray matter and 39.4% cerebellum). This increase of 40% agreed with the literature value (Hayashida et al., 1996). No significant difference in the amount of increase was observed among the regions (see Fig. 5B).

Figs. 6A–C show the results of comparison of rest–acetazolamide studies with SPECT and PET. The CBF images by both the Dual-Table ARG SPECT and $H_2^{15}O$ ARG PET methods were similar both quantitatively and qualitatively (Fig. 6A). The CBF values by the SPECT method showed the consistency with those by PET over the regions of deep and cortical gray matter (frontal, temporal, occipital gyri) and cerebellum (Fig. 6B), and this consistency resulted in the good correlation of CBF increase between PET and SPECT (Fig. 6C).

Discussion

In this study, we developed a new method of quantitative CBF mapping, which is based on the mathematical formulation for repeat CBF quantitation using a diffusible tracer that incorporates time-dependent changes of tissue radioactivity distribution, and showed that this method allows the test–retest assessment of quantitative CBF images within a reasonable scan

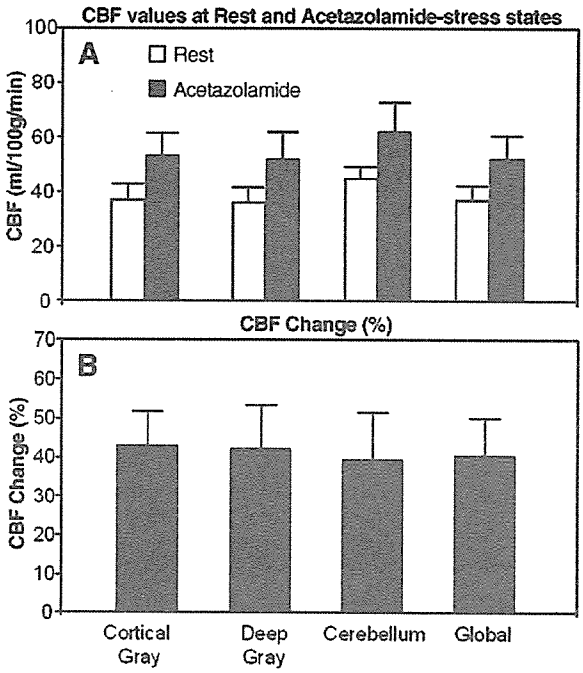

Fig. 5. (A) CBF values at both of rest and acetazolamide-stress states and (B) %change of CBF obtained from the rest–acetazolamide studies performed on the second group. The values of CBF and %change of three gray matter regions, namely the cortical and deep gray matter and cerebellum, and the whole brain regions, were summarized. No significant difference was observed in the %change among the regions.

interval. The noise enhancement, which has been a major restriction in previous approaches when using a simplified background subtraction technique, has been suppressed with the present approach.

Validity of this method has been demonstrated in sequential SPECT studies at rest and after acetazolamide in conjunction with a split-dose administration of IMP. IMP is a diffusible tracer with significant clearance from the brain over time (Kuhl et al., 1982; Iida et al., 1994a,b). It should, however, be noted that the kinetic behavior of IMP can be well described by a mathematical model (single-tissue compartment model). Thus, in this study, the formulation was given, based on the single-tissue compartment model, for a split-dose administration protocol, allowing the accurate quantitation of CBF at two physiological conditions. The quantitative accuracy and the precision of this approach at rest and after acetazolamide are acceptable in the clinical setting, allowing the rest–acetazolamide study to be carried out with a total study time of less than 1 h with an interval of 20 to 30 min between the two IMP administrations.

The new formulation that estimates the second CBF from the second SPECT scan by incorporating the background radioactivity from the previous scan into the formulation, has been validated successfully in this study with clinical scans. The calculated CBF images were consistent between the first and the second scans in the rest–rest study, in which image quality of the second CBF was not different from that from the first scan. In the previous work (Iida et al., 2000), we have evaluated the reproducibility of both CBF image in rest–rest study, using 160 square ROIs (34×34 mm^2) those were placed on brain region including gray and white matter of 5 tomographic slices of CBF images at axial position shown in Figs. 3A and 4A, and obtained the difference within 3%. In other study presented in domestic meeting (Annual meeting of Japanese Society of Nuclear Medicine (2000)), we have also compared the test–retest CBF image sets generated in rest–rest study by the presented method, with those by a traditional microsphere method (Kuhl et al., 1982), and found same reproducibility of the both test–retest CBF images for the both CBF calculation methods, with better quality of the second CBF image by the presented method than by the traditional method. Therefore, from these previous results showing enough accuracy of reproducibility over whole brain regions, we have focused the variation of CBF values in regions those have been interested in many clinical studies, rather than whole brain regions. The rest–acetazolamide study also demonstrated reasonable quality of CBF images both at rest and after acetazolamide. The estimated values of CBF at both rest and acetazolamide states, and %increase of CBF showed a good linear relationship with those by $H_2^{15}O$ PET, although there was a small offset in the comparison of %increase of CBF. This small bias was resulted from the slight underestimation of background radioactivity, which might be affected by reconstructed image with lower count statistics due to the fewer number of detector and relatively higher scatter fraction in the data acquired from dual-headed camera, compared to that of triple-headed camera (k_0=0.3000 for dual-headed and k_0=0.2141 for triple-headed). The amount of about 40% increase of CBF in healthy volunteers, however, agreed with the literature values, which also suggests validity of the present method (Hayashida et al., 1996).

The transient distribution of the tissue radioactivity concentration at the time of the second IMP injection can be accurately estimated from the first scan with the present method with minimal enhancement of statistical noise. It was shown that this estimated tissue radioactivity distribution was in a good agreement with that directly measured by a short (10 min or 5 min) SPECT scan, without enhancement of statistical noise (Fig. 3A). It is important to note that this agreement was confirmed not only in the rest–rest protocol (Fig. 3B), but also in the rest–acetazolamide protocol (Fig. 3C), in which the acetazolamide challenge was given during the 1st SPECT scan. This can be understood by referring to the approximate formulation of the transient contribution weight as defined in Eq. (3). As has been described in theory, the transient contribution is approximately proportional to the first-derivative of the tissue radioactivity concentration, and thus highly weighted only at the early phase after the tracer administration, but small after the peak of tissue radioactivity when a bolus administration protocol in employed. CBF changes some time after the immediate period post IMP injection have only a very small or negligible effect on the background activity. Eq. (2) also implies that the estimated CBF maps at rest and after acetazolamide are highly weighted to the early period immediately after each of IMP administrations, which has been shown in the previous study using simulation (Iida et al., 2000). From these findings, it can be expected that the second CBF should yield the elevated CBF values even though CBF is decreased after a certain period such as >10 min after the 2nd IMP administration.

In general, kinetic analysis in PET or SPECT assumes a constant physiological condition throughout the whole study period, and only a single set of physiological parameters such as CBF is typically estimated from a series of data. The temporal resolution of the PET/SPECT methodology has therefore been